JOURNAL OF APPLIED CRYSTALLOGRAPHY

ISSN 1600-5767

Received 10 August 2016
Accepted 12 September 2016

Edited by K. Chapman, Argonne National Laboratory, USA

Keywords: X-ray powder diffraction; neutron powder diffraction; diffuse scattering; refinement; stacking faults; planar defects; layered materials; *FAULTS*; *DIFFaX*; battery materials; manganese oxide.

Supporting information: this article has supporting information at journals.iucr.org/j

FAULTS: a program for refinement of structures with extended defects

Montse Casas-Cabanas,[a]* Marine Reynaud,[a] Jokin Rikarte,[a] Pavel Horbach[b,c] and Juan Rodríguez-Carvajal[b]*

[a]CIC Energigune, Parque Técnologico de Álava, Albert Einstein 48, Miñano, 01510, Spain, [b]Institut Laue–Languevin, 71 avenue des Martyrs, Grenoble, 38000, France, and [c]Institute for Metal Physics, National Academy of Science, 36 Vernadsky Boulevard, Kiev, 03680, Ukraine. *Correspondence e-mail: mcasas@cicenergigune.com, jrc@ill.fr

The *FAULTS* program is a powerful tool for the refinement of diffraction patterns of materials with planar defects. A new release of the *FAULTS* program is herein presented, together with a number of new capabilities, aimed at improving the refinement process and evolving towards a more user-friendly approach. These include the possibility to refine multiple sets of single-crystal profiles of diffuse streaks, the visualization of the model structures, the possibility to add the diffracted intensities from secondary phases as background and the new *DIFFaX2FAULTS* converter, among others. Three examples related to battery materials are shown to illustrate the capabilities of the program.

1. Introduction

FAULTS is a profile refinement program that has been developed to analyse the diffraction patterns of materials with planar defects. It is based on the *DIFFaX* simulation program developed by Treacy *et al.* (1991), which has been extended to allow the refinement of all the parameters involved in the calculation of *DIFFaX* diffracted intensities of powder patterns through a minimization process. A similar software was independently developed by Leoni *et al.* (2004). Additionally, *FAULTS* includes several modules from the Crystallographic Fortran Modules Library (CrysFML; Rodríguez-Carvajal & Gonzalez-Platas, 2003*a*,*b*).

The program *FAULTS* behaves like a Rietveld refinement program in which the model for calculating the profile intensities is not a simple crystallographic three-dimensional periodic structure. The minimized function with respect to the set of free parameters collected in the array $\boldsymbol{\alpha}$, like in the Rietveld method, is

$$\chi^2 = \sum_{i=1}^{n} w_i \left[y_i - y_{c,i}(\boldsymbol{\alpha}) \right]^2, \qquad (1)$$

in which the calculated profile intensity at the point i, $y_{c,i}(\boldsymbol{\alpha})$, is the convolution of the theoretically calculated intensity with the resolution function of the diffractometer, and w_i is the inverse of the variance of the observed profile intensity y_i (see Appendix *A* for details).

Since the release of the first version (Casas-Cabanas, Rodríguez-Carvajal & Palacín, 2006), the *FAULTS* program has been successfully used for the refinement of many complex faulted structures (see *e.g.* Casas-Cabanas, Rodríguez-Carvajal, Canales-Vázquez & Palacín, 2006, Casas-Cabanas *et al.*, 2007; O'Malley, 2009; Kiefer *et al.*, 2011; Knížek *et al.*, 2015; McCalla, Abakumov, Saubanère *et al.*, 2015; McCalla,

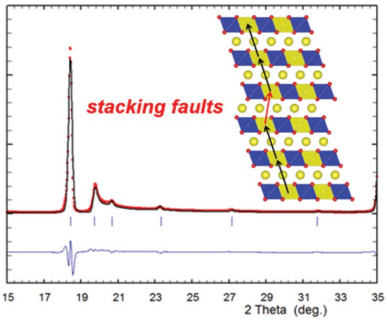

Abakumov, Rousse *et al.*, 2015; Matsunaga *et al.*, 2016*a*,*b*; Shunmugasundaram *et al.*, 2016). An upgraded version of the original code, which includes a number of new features, is herein presented together with three examples. Among the novel features is the use of the Levenberg–Marquard algorithm for minimization (instead of the simplex and simulated annealing methods used in the previous version), which allows a considerable speed-up of the computation time. Other useful new features include the visualization of the model structures with the program *FullProf Studio* (Rodríguez-Carvajal & Chapon, 2004) or with *VESTA* (Momma & Izumi, 2011), the possibility to include the diffracted intensities from secondary phases as background, the refinement of background points when treated as a polynomial, and the automatic conversion of *DIFFaX* input files into *FAULTS* format using the *DIFFaX2FAULTS* converter. We have also included the possibility to refine multiple reciprocal lattice scans of single crystals presenting defects.

Since the program has been completely reworked, three examples are shown here to illustrate some of the new features of *FAULTS*, and the corresponding input files are provided as supporting information. The first example deals with the simulation of O1-type stacking faults in the O3-type structure of Li_xNiO_2 ($x < 0.3$) (Croguennec *et al.*, 2000*a*,*b*, 2001). This material was studied as a cheaper alternative to $LiCoO_2$ in Li-ion batteries and was found to undergo an O3 (AB CA BC oxygen stacking) to O1 (AB AB oxygen stacking) transition upon Li^+ extraction. Since slab gliding is at the origin of this transition, stacking faults are formed, leading either to O3 domains with local O1 stacking faults or to O1 domains with local O3 stacking faults. The diffraction pattern of O3-Li_xNiO_2 with O1 structural defects has been simulated using *FAULTS*, and the resulting pattern has been refined in order to test the robustness of the new version of the program.

The second example refers to the related compound Li_2PtO_3, isostructural to Li_2MnO_3 electrode material, which also crystallizes in a layered structure with stacking disorder. The *FAULTS* refinement of its experimental diffraction pattern (Casas-Cabanas *et al.*, 2007) has been revisited using the new features included in this updated version of *FAULTS* and a more realistic description of its defect structure has been obtained.

The third example demonstrates that *FAULTS* is not restricted to characterizing only layered structures but it is rather intended for any structure that presents planar defects (including three-dimensional frameworks). In this case, we have refined the experimental X-ray diffraction (XRD) pattern of a γ-MnO_2 sample which is used in commercial alkaline primary batteries. Although the details of the structural arrangements of these electrode materials could be of particular interest to correlate with their battery performance, there has been up to now no method to characterize properly their structural features. In fact, the X-ray patterns of the electrochemically active MnO_2 are usually of rather poor quality and consist of a small number of sharp and broad lines. A few patterns match more or less accurately that of the pyrolusite mineral (rutile-type structure), while most exhibit a strong resemblance to the diffraction pattern of ramsdellite (de Wolff, 1959; Chabre & Pannetier, 1995). Herein we demonstrate that the details of the structural arrangements of these MnO_2 materials can now be determined accurately using *FAULTS*.

The upgraded version of *FAULTS* can be freely downloaded (see §5) to study these and other materials, for which the exact determination of the parameters specific to their different types of defects is essential to understand their physical-chemical properties.

2. New features of *FAULTS*

2.1. Input file

The first step of any refinement using the program *FAULTS* consists in defining a relevant set of layers to be stacked one on top of the other through stacking vectors with certain probabilities to describe the (ideal or faulted) structure. These structural parameters, together with instrumental considerations, are given in a free-format input data file, similar to that of *DIFFaX*. The input file is created manually, although the *DIFFaX2FAULTS* converter can now be used to adapt existing *DIFFaX* input files.

Some new refinable parameters have been included in the instrumental section to model experimental diffraction data more accurately. These include λ_2 and the intensity ratio I_2/I_1, zero shift, and other systematic 2θ shifts with $\sin\theta$ or $\cos\theta$ dependence (sample transparency coefficient and sample displacement in θ–2θ diffractometers, respectively). As in the first version of the program, the broadening of the theoretical diffraction patterns is done by convoluting numerically with a Voigt function using the approximation of Thompson–Cox–Hastings (Thompson *et al.* 1987). See Appendix *A* for details.

The input file contains now several new optional subsections. The first one allows the description of an average unit cell to generate all the Bragg positions in the output plot of calculated and experimental patterns in the form of vertical sticks, although this average unit cell is not used for the pattern calculation. This option has been included for those cases in which the cell parameters used in the *FAULTS* description of the structure are different from those of the original cell.

Another optional subsection is the possibility to generate an output file suitable for *FullProf Studio* or *VESTA* to visualize the model structure of the *FAULTS* input file. In this subsection the user can decide how many layers and the exact sequence to be plotted, which is particularly useful to validate the model and avoid errors in the description of the crystal structure and the corresponding stacking faults.

2.2. Background and secondary phases

The background can now be modelled as a polynomial of refinable coefficients or can be subtracted after being modelled by a linear interpolation of background points given in a separate input file as in the first version of *FAULTS*.

Moreover, secondary phases can be included in the calculated pattern if separate free-format pattern files are provided together with their refinable scale factors. The calculation of the patterns corresponding to secondary phases can be done straightforwardly by using *FullProf* (Rodríguez-Carvajal, 1993*a*,*b*) or any other Rietveld program that allows the calculation of theoretical diffraction patterns. Thus, they will be treated as background. A list of reflections for each of the secondary phases can optionally be provided so as to include them in the output plot of calculated and experimental patterns in the form of vertical sticks. The program delivers the phase fraction of each secondary phase, which is calculated as the ratio of the diffracted area corresponding to each phase and, therefore, is only valid provided that the composition and density of the main and secondary phases are the same. In the case of impurity phases of heterogeneous compositions a true quantitative phase analysis is not currently possible. The reason is that the lack of periodicity in the faulted phase makes it complicated to put the scale factors on a common footing. We are presently exploring the generation of the calculated pattern with *FullProf* using a scale factor that may be used together with the scale factor and average density and composition of the faulted phase in order to perform a true quantitative phase analysis.

2.3. Minimization algorithm

The minimization algorithm has now been changed from the simplex and simulated annealing methods used in the initial versions of *FAULTS* to the Levenberg–Marquard Algorithm (LMA). This LMA calculation, also known as the damped least-squares method, is a robust local minimization method that allows a faster refinement. LMA does not take into account boundary conditions and therefore the option of giving upper and lower limits for the refinable parameters has been suppressed.

This algorithm is applied to both single-crystal Q scans and powder diffraction patterns. In the case of single-crystal scans in reciprocal space, one can use several data files with different reciprocal space directions simultaneously (see the manual for details).

2.4. Output files

When a simulation is to be performed, the program creates an output file either with the calculated powder pattern, with streak patterns in the reciprocal space of a single crystal, or with the calculated selected area diffraction pattern. The former are free-format files that can be plotted with any graphical interface (*WinPLOTR* can handle both directly; Rodríguez-Carvajal & Roisnel, 1998; Roisnel & Rodríguez-Carvajal, 2001), while the latter is an unsigned 16-bit image of size 256 × 256. A progress report that contains a summary of the information on the structural model read by *FAULTS* is also generated.

When a refinement process is launched, the first output file created at the end of the process contains the observed and calculated profiles, together with the difference and the Bragg reflections if an average cell has been described in the input file (which will correspond either to the *FAULTS* unit cell or to the average cell if included). Additionally, *FAULTS* generates a progress report with the values of each refinable parameter during the refinement process, and a new input file in which the refined values of each refinable parameter have already been updated so that it can now be used as input file to continue with the refinement process.

In all cases, if the user has specified commands for the drawing of the structural model, the program will create a file to be fed into the visualization program *FullProf Studio* or *VESTA*.

3. Case studies

3.1. $Li_xNi_{1.02}O_2$ example

$LiNiO_2$ has been extensively studied as a replacement for isostructural $LiCoO_2$ as an Li-ion positive electrode material owing to its lower cost and higher practical capacity. Both crystallize in a structure consisting of three NiO_2 slabs per unit cell, with an AB CA BC oxygen stacking sequence and lithium ions located in the octahedral sites of the interlayer spaces ($R\bar{3}m$ space group, O3 structural type according to Delmas' notation; Delmas *et al.*, 1980) (see Fig. 1*a*). $Li_{1-x}Ni_{1+x}O_2$ is usually obtained since there is a tendency towards loss of lithium and nickel reduction to Ni^{II+} (Rougier *et al.*, 1996). The excess nickel is located in the lithium layers owing to the similarity in size to lithium, resulting in poor electrochemical performance (Ohzuku *et al.*, 1993; Delmas *et al.*, 1997). Lithium can be reversibly extracted from/inserted into the

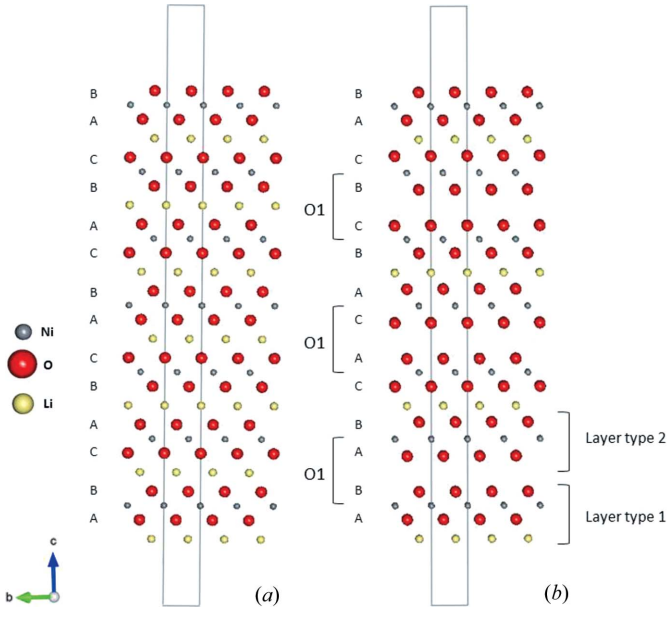

Figure 1
(*a*) Ideal structure of $LiNiO_2$ with O3 stacking and (*b*) proposed structural model for $Li_xNi_{1.02}O_2$ with O1 stacking faults as visualized using *FullProf Studio* (Rodríguez-Carvajal & Chapon, 2004). Grey, red and yellow balls represent the nickel, oxygen and lithium atoms, respectively.

Table 1
Starting and final values of the parameters refined in the analysis of the simulated data of $Li_xNi_{1.02}O_2$.

		Refinement	
Refined parameters	Simulation	Initial values	Final values (standard deviation)
a, b (Å)	2.81540	2.86540	2.81635 (5)
c (Å)	13.36300	13.26300	13.3643 (6)
zO_1	0.07133	0.17133	0.0722 (1)
zO_2	−0.07133	−0.17133	−0.0722 (1)
zO_3	0.07133	0.17133	0.0984 (6)
zO_4	−0.07133	−0.17133	−0.0984 (6)
α_{12}, α_{23}, α_{31}	0.85800	1.00000	0.8631 (6)
α_{14}, α_{25}, α_{36}	0.14200	0.00000	0.1369 (6)
α_{42}, α_{53}, α_{61}	0.85800	1.00000	0.879 (4)
α_{44}, α_{55}, α_{66}	0.14200	0.00000	0.121 (4)

structure concomitant to several phase transitions that occur through slab gliding. In particular, highly deintercalated $Li_xNi_{1.02}O_2$ ($x < 0.3$) also crystallizes in an O3-type layered structure (Croguennec *et al.*, 2001). In *FAULTS*, this can be described with three structurally identical layers (Layer 1, Layer 2 and Layer 3), containing an NiO_2 slab and a lithium interslab, but shifted with respect to each other by the transition vectors $\mathbf{t}_{12} = \mathbf{t}_{23} = \mathbf{t}_{31} = (2/3\ 1/3\ 1/3)$, with a stacking probability of 1 for each transition.

A second phase, with AB oxygen stacking sequence (O1 structural type), is also formed at low Li content (Croguennec *et al.*, 2001). For the O3 phase, as soon as lithium ions are removed from the interslab space, O1-type faulting occurs locally. The real structure of the O3 phase has thus been proposed to consist of 5% O1 stacking faults in the O3 structure from *DIFFaX* simulations (Croguennec *et al.*, 2001).

In *FAULTS*, these defects require the definition of a new type of layer, structurally different since these layers do not contain any lithium. Therefore, three more layers (Layer 4, Layer 5 and Layer 6) are defined in the faulted structure, structurally identical to each other but different from the previous ones, and new transitions [$\mathbf{t}_{14} = \mathbf{t}_{25} = \mathbf{t}_{36} = (0\ 0\ 1/3)$] are allowed in order to describe the defects (see Fig. 1*b*).

By means of the structural model described above, *FAULTS* was first used to simulate a diffraction pattern of a defective $Li_xNi_{1.02}O_2$ structure with the parameter values described in Table 1. The background, number of counts and Poisson noise were generated using an offset value of 150.0 and a scale factor of 1.0. Then, in a second stage, the obtained simulated XRD pattern was used as input data to be refined in order to analyse and test the program. The initial values of the parameters to be refined in the starting structural model were chosen to be far enough from the correct ones so as not to bias the results, as shown in Table 1 and Fig SI1 (in the supporting information). The refinement was done by means of the LMA minimization algorithm, restraining the program to a maximum of 2400 function evaluations and a criterion of convergence of a difference between consecutive χ^2 of less than 10^{-5}. The starting R_p and χ^2 values were 45.62% and 186.38, respectively, and at the end of the refinement the final values were 4.86% and 1.03, respectively, with a refinement duration of 1 min and 55 s (using an Intel Core i5-3470S processor CPU at 2.90 GHz with 4.00 GB of RAM). Fig. 2 presents a visual comparison between the calculated and the simulated powder patterns and their difference, and Table 1 compares the initial and final values of the refined parameters. The values of the refined parameters are very close to those used in the simulation and lead to an XRD pattern practically identical to the simulated one (Fig. 2). The evolution of the a and b cell parameters and of χ^2 and R_p throughout a run of 12 iteration cycles is shown in Fig. 3. The plot shows the convergence of the cell parameter values towards the value used in the simulation and the concomitant decrease of R_p and χ^2.

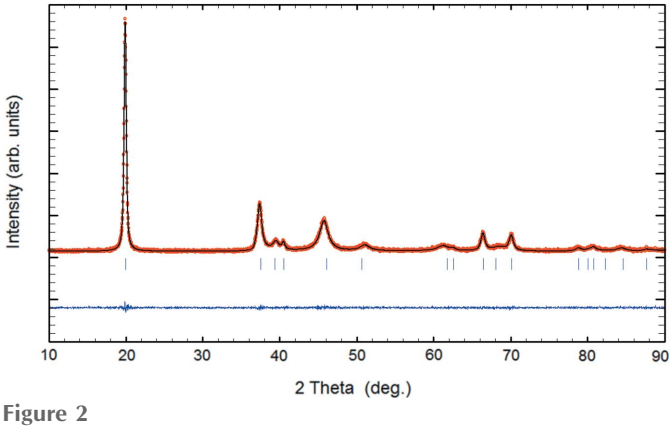

Figure 2
Comparison of the X-ray diffraction patterns corresponding to the *FAULTS* analysis of the simulated data of $Li_xNi_{1.02}O_2$: simulated pattern (dotted red curve) and calculated pattern using the *FAULTS* refinement (continuous black curve). The curve underneath shows the difference between them. The vertical bars show the positions of the Bragg reflections of the $R\bar{3}m$ average unit cell (the one used to describe the ideal O3 structure of $LiNiO_2$).

3.2. Li_2PtO_3 example

Similarly to the previous example, the structure of Li_2PtO_3 (whose formula can also be written as $Li[Li_{1/3}Pt_{2/3}]O_2$) can be

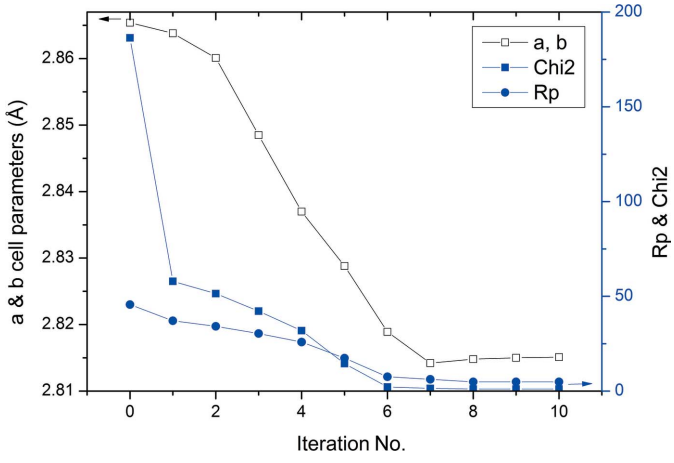

Figure 3
Evolution of the cell parameters a and b and of the agreement factors R_p and χ^2, as a function of the cycle number during the refinement of the simulated data of $Li_xNi_{1.02}O_2$.

described as $[Li_{1/3}Pt_{2/3}]O_2$ slabs with lithium ions located in the interlayer space. In this case, however, lithium and platinum atoms of the same slab exhibit in-plane order in the form of a honeycomb owing to their different size (Fig. 4*a*), which results in the appearance of superstructure reflections in the diffraction pattern, especially in the region $2\theta = 17$–32°. These superstructure reflections often appear broadened and adopt the so-called Warren shape, which is indicative of significant stacking disorder. The ideal structure can be indexed using the *C*2/*m* space group (Casas-Cabanas *et al.*, 2007; O'Malley *et al.*, 2008) and cell parameters a = 5.190 (4), b = 8.983 (2), c = 5.112 (3) Å and β = 109.9 (1)° (Fig. 4*b*). This description is usually used for most Li_2MO_3 materials (M = transition metal) (Charenton & Strobel, 1988; Bréger *et al.*, 2005; O'Malley *et al.*, 2008; Boulineau *et al.*, 2009), although this simplified description does not take into account the particular features along the stacking direction.

In previous work (Casas-Cabanas *et al.*, 2007) the experimental X-ray diffraction pattern of an Li_2PtO_3 sample was refined using the first version of the *FAULTS* program. The real structure was described using the *FAULTS* program with a structural model built using four different layers: three structurally identical layers containing lithium and platinum atoms and a fourth layer with the rest of the lithium and oxygen atoms. The three identical layers were required to describe the rotational displacements (0, 1/3, 0) and (0, −1/3, 0) that were found to be at the origin of stacking faults and that were included in terms of stacking transition vectors (Figs. 4*c* and 4*d*). In order to gain computational speed, the cell was transformed into a smaller primitive triclinic unit cell with cell parameters a = 5.1874, b = 5.1874, c = 5.1123 Å, α = 80.193, β = 99.807, γ = 60.039° obtained from the transformation: $\mathbf{a}' = 1/2(\mathbf{a}+\mathbf{b})$, $\mathbf{b}' = 1/2(\mathbf{a}-\mathbf{b})$, $\mathbf{c}' = \mathbf{c}$ (Fig. 4*b*). Our best fit was obtained for a sample with similar stacking probabilities for the three types of Li/Pt layers (39.5, 30.4 and 30.1%), but an explicit sequence of layers was needed in order to avoid excessive broadening of the peaks at 2θ = 20–25°. Since it is unlikely that all measured particles share the same stacking sequence, the refinement has now been re-examined with the current version of the program [see Casas-Cabanas *et al.* (2007) for experimental details of the Li_2PtO_3 sample]. A two-phase model has now been used by including a defect-free secondary phase. As previously mentioned, free-format pattern files that are linked to a refinable scale factor can be read and included as background in *FAULTS*. This secondary phase would be at the origin of the sharpness of superstructure reflections despite having a pronounced Warren fall caused by the defects of faulted particles.

As in our previous refinement the smaller primitive cell was used and a new cell c parameter had to be calculated (c'' = 4.8069 Å) in order to have the stacking direction perpendicular to the a and b axes, which in turn requires the correction of atomic positions and stacking vectors with an additional shift vector. In this model, however, a recursive stacking sequence with an infinite number of layers was used to model the faulted structure. The background was modelled by linear interpolation of selected points, and two additional patterns

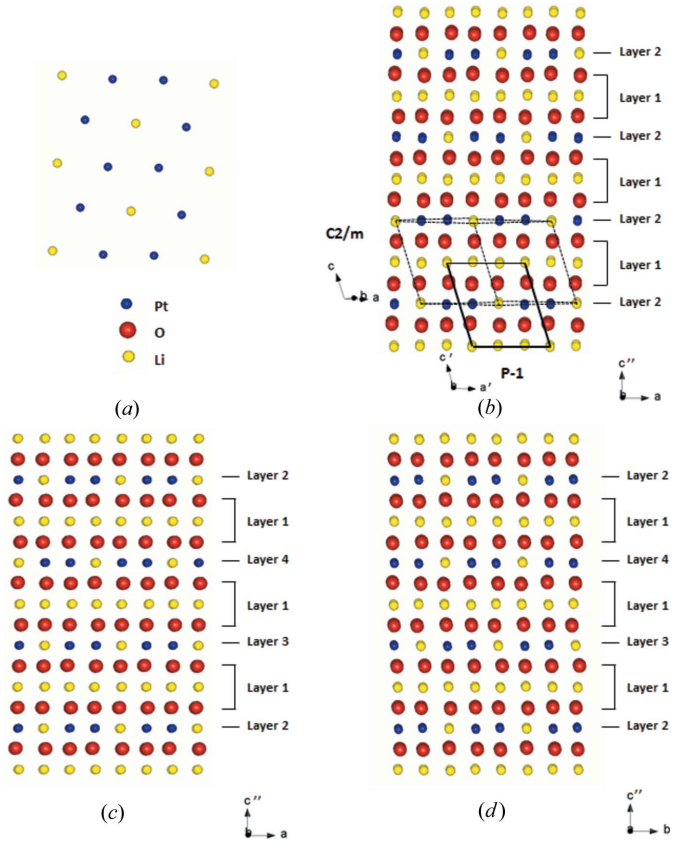

Figure 4
(*a*) Li/Pt structural layer in Li_2PtO_3 where the honeycomb ordering can be visualized. (*b*) Ideal Li_2PtO_3 structure where *C*2/*m* and $P\bar{1}$ unit cells can be viewed as well as the stacking sequence used in *FAULTS* to describe the structure. (*c*), (*d*) Hypothetical structure for Li_2PtO_3 following the stacking sequence 1 2 1 3 1 4 1 2 viewed from the *b* and *a* axes, respectively. All structures were drawn using *FullProf Studio* (Rodríguez-Carvajal & Chapon, 2004).

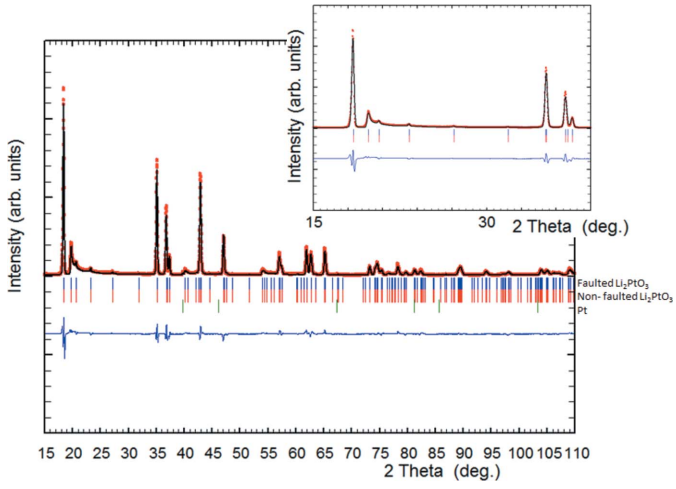

Figure 5
Comparison of the X-ray diffraction patterns corresponding to the *FAULTS* analysis of Li_2PtO_3: experimental pattern (dotted red curve) and calculated pattern using the *FAULTS* refinement (continuous black curve). The curve underneath shows the difference between them. The inset is an enlargement of the patterns at low 2θ, showing the good fit of the superstructure reflections.

Table 2
Refined structural model of the sample of Li_2PtO_3.

Cell: a' = 5.18616 (5), b' = 5.18616 (5), c'' = 4.81316 (3) Å, α = 90, β = 90, γ = 60.030 (1)°.

Layers.

	Atom	x/a'	y/b'	z/c''	B_{iso} (Å^2)	Occupancy
Layer 1	Li^{I+}	0	0	0	0.7	1.0
	Li^{I+}	0.35 (5)	0.35 (2)	0	0.7	1.0
	Li^{I+}	0.660 (2)	0.660 (4)	0	0.7	1.0
	O^{II-}	−0.042 (8)	0.68 (1)	0.25 (2)	0.1	1.0
	O^{II-}	0.35 (2)	0.04 (3)	0.24 (4)	0.1	1.0
	O^{II-}	0.709 (5)	0.28 (2)	0.240 (6)	0.1	1.0
	O^{II-}	0.046 (1)	0.32 (3)	−0.25 (1)	0.1	1.0
	O^{II-}	0.654 (9)	−0.04 (1)	−0.24 (1)	0.1	1.0
	O^{II-}	0.295 (6)	0.72 (2)	−0.244 (3)	0.1	1.0
Layer 2 = 3 = 4	Pt^{IV+}	0.834 (2)	0.841 (1)	0	0.1	1.0
	Pt^{IV+}	0.167 (2)	0.157 (1)	0	0.1	1.0
	Li^{I+}	0.500	0.500	0	0.7	1.0

Transition vectors.

	Transition	x/a'	y/b'	z/c''	Probability	Type
From layer T1	T1 → T1	–	–	–	0	Forbidden
	T1 → T2	−0.1677 (2)	0.1670 (5)	$\frac{1}{2}$	0.635 (1)	
	T1 → T3	0.178 (3)	0.4799 (3)	$\frac{1}{2}$	0.146 (1)	
	T1 → T4	0.492771	0.848048	$\frac{1}{2}$	0.219 (1)	
From layer T2	T2 → T1	0.493 (2)	0.8480 (2)	$\frac{1}{2}$	1	
	T2 → T2	–	–	–	0	Forbidden
	T2 → T3	–	–	–	0	Forbidden
	T2 → T4	–	–	–	0	Forbidden
From layer T3	T3 → T1	0.178 (3)	0.4799 (3)	$\frac{1}{2}$	1	
	T3 → T2	–	–	–	0	Forbidden
	T3 → T3	–	–	–	0	Forbidden
	T3 → T4	–	–	–	0	Forbidden
From layer T4	T4 → T1	0.493 (2)	0.8480 (2)	$\frac{1}{2}$	1	
	T4 → T2	–	–	–	0	Forbidden
	T4 → T3	–	–	–	0	Forbidden
	T4 → T4	–	–	–	0	Forbidden

were included as separate files to be added as background in order to account for secondary phases: defect-free Li_2PtO_3 to describe a material consisting of a mixture of faulted and non-faulted particles (or areas); and Pt, since the studied sample contained small residual amounts of precursor. These files were generated using the *FullProf* program using the same cell parameters as the *FAULTS* refined structure for the former, and PDF file number 4-802 for the latter. A total of 39 independent parameters were simultaneously refined, including scale factors for each of the different phases, cell parameters, atomic positions (except for B_{iso}, which were fixed to the values obtained from the Rietveld refinement), stacking probabilities and stacking vectors. The final refinement results using this alternative model are shown in Table 2 and Fig. 5. The calculated phase fraction of the faulted material is ∼77.3%. The refined stacking probabilities of this phase describe a structure with a majority of ideal stacking sequences, represented by transitions from layer 1 to layer 2, with a refined probability of 63.5%; nevertheless, stacking faults are significant, represented by transitions from layer 1 to layers 3 and 4, with a probability of 14.6 and 21.9% respectively. The goodness of the refinement is supported by the final figure of merit R factor = 10.32% which is lower than that of our previous refinement thanks to the use of secondary phases and the combination of a faulted and a non-faulted phase of similar structure. This new model describes well the experimental XRD data and is more plausible than the explicit stacking sequence used in our previous refinement (Casas-Cabanas *et al.*, 2007).

3.3. MnO_2 example

Manganese oxide, MnO_2, is probably one of the metal oxides that show the largest structural complexity, as widely discussed by Chabre & Pannetier (1995) in their extensive review on this kind of material and by other authors in more recent reports (Jouanneau *et al.*, 2001; Balachandran *et al.*, 2003; Kim *et al.*, 2006; Hahn *et al.*, 2013). Manganese oxides exhibit a diverse range of compositions and polymorphs. The forms usually classified as γ- and ε-MnO_2 are the electrochemically active forms of manganese oxide, which are commonly used in battery applications. Generally, a few diffraction patterns of these manganese oxides match more or less accurately that of the pyrolusite mineral (rutile-type structure), while most exhibit a strong resemblance to the diffraction pattern of ramsdellite.

Both the pyrolusite and the ramsdellite structures present a distorted hexagonal close packed array of oxygen atoms, in which half of the octahedral sites are occupied by manganese +IV. The two structures differ only in the arrangement of the manganese atoms (Figs. 6*a* and 6*b*). The pyrolusite structure presents single chains of edge-sharing MnO_6 octahedra running along the *b* axis; each chain is connected to four other chains through the corners of its MnO_6 octahedra. Conversely, the ramsdellite structure is built on double chains of edge-sharing MnO_6 octahedra. As a result, the atomic arrangements of the two structures are very similar in the *a*- and *b*-axis directions; the difference resides in the arrangement along the *c* axis.

On the basis of this observation, de Wolff proposed in 1959 to describe the structure of poorly crystallized samples of γ-MnO_2 as an irregular intergrowth of pyrolusite and ramsdellite elements (de Wolff, 1959). An illustration of a hypothetical structure of this kind is given in Fig. 6(*c*). Such an atomic arrangement, which would be later named 'de Wolff disorder' by Chabre & Pannetier (1995), implies the absence of long-range ordering along the **c** direction and explains why the structure of these materials is not directly attainable by conventional treatment of powder diffraction data. In 1995, Chabre and Pannetier presented a pseudo-quantitative interpretation of the XRD patterns of different MnO_2 materials based on the comparison of experimental data with numerical simulation using the *DIFFaX* program (Treacy *et al.*, 1991; Chabre & Pannetier, 1995). They confirmed that most of the polymorphs of manganese oxides (*i.e.* natural, chemically prepared, electrochemically prepared γ- and ε-MnO_2) can be described as ramsdellite-type compounds containing various

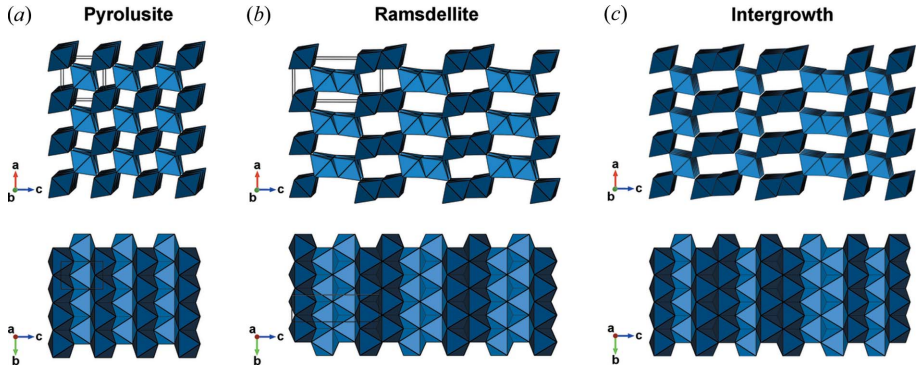

Figure 6
Illustration of the (*a*) pyrolusite and (*b*) ramsdellite structures, and of (*c*) a hypothetical intergrowth of pyrolusite (single chains) and ramsdellite (double chains) elements (de Wolff disorder). The MnO_6 octahedra are coloured with two different blues, denoting two different coordinates of the Mn site along the *a* axis (0 and $\frac{1}{2}$, respectively).

numbers of de Wolff defects and/or amounts of microtwinning, while heat-treated samples of MnO_2 were better described as pyrolusite frameworks including random ramsdellite defects (Chabre & Pannetier, 1995). However, the authors concluded their study by stating that their analytical 'approach could be improved and alleviated by developing dedicated profile refinement techniques, analogous to the Rietveld method'. Below, we show that *FAULTS* responds to this open call and enables us to extract quantitative information about the intergrowth of pyrolusite and ramsdellite motifs.

A powder sample of MnO_2 used in commercial primary batteries was kindly provided by the company SAFT (Bordeaux, France). The sample consisted of a fine black powder. Scanning electron microscopy (SEM) observations, performed with an FEI QUANTA 200FEG equipped with an EDAX probe, showed that it was constituted of micrometric aggregates of smaller particles, whose sizes ranged from 20 to 200 nm. An X-ray powder diffraction pattern of the sample was recorded in the range $10 \leq 2\theta \leq 120°$ (step size 0.03°) using a Bruker D8 Advance diffractometer in Bragg–Brentano θ–θ configuration, equipped with Cu $K\alpha$ radiation (λ_1 = 1.5406 Å and λ_2 = 1.5444 Å) and a LYNXEYE detector, operated with discrimination. Fig. 7 compares the experimental XRD pattern of the sample with the simulated patterns of the pyrolusite and ramsdellite structures [ICSD collection codes No. 73716 (Bolzan *et al.*, 1993) and No. 171866 (Post & Heaney, 2004), respectively], which were calculated with the program *FullProf*. The experimental pattern of the MnO_2 sample shows similarities with that of the pyrolusite structure, but exhibits significant anisotropic broadening and additional reflections, which suggest the existence of de Wolff defects. Indeed the pattern cannot be refined with a conventional Rietveld refinement, even using anisotropic models of size or strains (Fig. SI2). We performed a *FAULTS* refinement of the XRD data to extract relevant information about the structural details of this material.

The structural model used to start the *FAULTS* refinement was built from the published structures of pyrolusite and ramsdellite [ICSD collection codes No. 73716 (Bolzan *et al.*, 1993) and No. 171866 (Post & Heaney, 2004), respectively]. Both published structures were first transformed to define the *c* axis parallel to the stacking direction (Figs. 6*a* and 6*b*). Then, each structure was described as a set of two layers with respect to a unique set of orthogonal vectors, whose norms were chosen to be *a* = 4.4041, *b* = 2.8765, *c* = 4.4041 Å (Fig. 8 and Table SI1). This set of vectors corresponds to the unit cell of the pyrolusite structure. By analogy with the notation previously used by Chabre & Pannetier (1995), the layers were

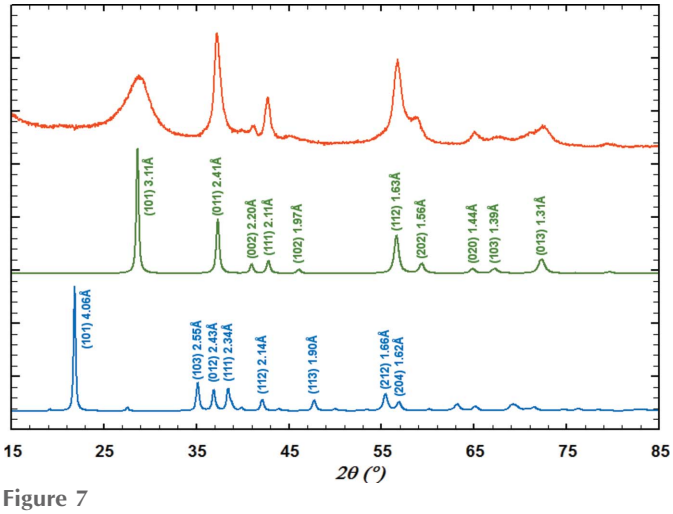

Figure 7
Comparison of the XRD pattern of the commercial sample of MnO_2 (red) with the simulated XRD patterns of the ideal pyrolusite (green) and ramsdellite (blue) structures. The Bragg indices and interreticular distances corresponding to selected reflections are indicated.

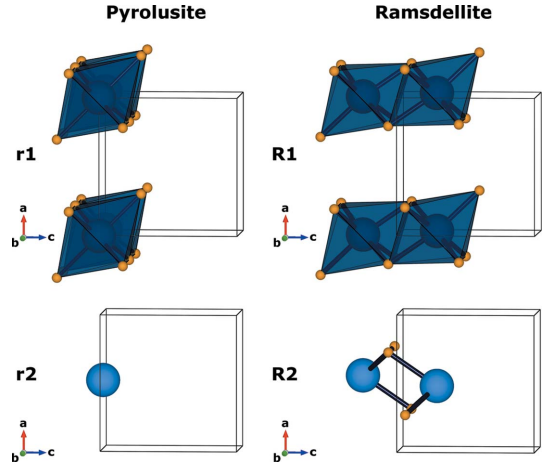

Figure 8
Illustrations of the four types of layers (r1, r2, R1 and R2) used in the *FAULTS* refinement. Blue and orange spheres represent the manganese and oxygen atoms, respectively.

denoted r1 and r2 for the two pyrolusite-type layers and R1 and R2 for the ramsdellite-type ones; it should be noted that our structural description of the layers is not strictly the same as theirs although it is equivalent. The transitions vectors, which describe the way the layers are vertically stacked, were defined so as to obtain the ideal pyrolusite and ramsdellite structures from the stacking sequences r1–r2–r1–r2$\cdots$ and R1–R2–R1–R2$\cdots$, respectively. On the other hand, the transition vectors used to switch from a pyrolusite layer to a ramsdellite layer, and the reverse, were chosen so as to place the manganese atom of the top layer at the position that would be occupied by the manganese atom in an ideal stacking. Examples of resulting structures are shown in Fig. SI3. For ease of comparison, we employ herein the same notations and statistical tools as proposed by Chabre & Pannetier (1995) to describe the stacking sequence of the two kinds of layers; the definitions of these statistical tools are reviewed in the supporting information. For both the simulations and the refinement presented below, the layer width and the number of layers stacked were taken as infinite and size effects were only modelled with D_G and D_L parameters (see Appendix *A*). No improvement of the refinement was obtained when working with anisotropic size broadening parameters, which is in agreement with the three-dimensional nature of the structure of manganese oxides (as opposed to layered materials). Finally, the stacking of the layers was treated as a recursive sequence of layers, which means that the diffracted intensities were calculated for a statistical ensemble of crystallites: each with a distinct stacking sequence, but weighted by the probability that such a sequence occurs.

Given the structural complexity and the considerable number of different stacking possibilities, we started our study by generating the simulated patterns of different stacking models in order to find out the general trends of evolution of the patterns as a function of the type of defect included. We analysed six different models that explore different restrictions in the stacking probabilities or different local motifs [some of them were already discussed by Chabre & Pannetier (1995)] and the results obtained are presented in the supporting information (Figs. SI4–SI9). The qualitative comparison of these simulated patterns with the experimental XRD pattern of the MnO_2 sample permitted us to establish that the latter was probably mainly constituted of pyrolusite domains with small random inclusions of ramsdellite motifs (*i.e.* probability of having a ramsdellite layer after a rutile one of approximately $P_{r\cdot R} \simeq$ 5–10%; models 5 and 6 in the supporting information).

At this stage, and using model 6 as starting point, we started the refinement of the experimental XRD pattern of the MnO_2 sample using the program *FAULTS*. The initial values of stacking probabilities $P_{r\cdot r}$ and $P_{R\cdot r}$ (*i.e.* having a pyrolusite layer after either a pyrolusite or a ramsdellite one, respectively) were thus chosen to be 90%, so that to start with the $(101)_r$ reflection at $d \simeq 3.11$ Å ($2\theta_{Cu} \simeq 28.7°$) sufficiently broadened.

In a first phase, we initially refined the zero shift, the cell parameters and the probabilities of transitions (P) in order to properly index all the reflections. Then, we introduced some isotropic broadening (parameters D_L and D_G and later U) to better fit the actual shape of the experimental peaks. Finally, we refined the atomic positions, transition vectors, atomic displacement parameters and background.

The results of the refinement are presented in Table 3 and Fig. 9. Selected Mn–O distances are given in Table SI2. The goodness of the refinement is supported by the final figures of merit R factor = 5.56% and χ^2 = 3.36. One can remark that all the experimental reflections are well indexed and that the broadening of each of them is well simulated. Note in particular the good position and intensity calculation of the tiny peaks $(001)_r$ at $d \simeq 4.44$ Å ($2\theta_{Cu} \simeq 20.3°$), $(002)_r$ at $d \simeq 2.24$ Å ($2\theta_{Cu} \simeq 40.0°$) and $(200)_r$ at $d \simeq 2.22$ Å ($2\theta_{Cu} \simeq 41.1°$), which were very badly assigned in the starting model. This refinement eventually led to a structural model based on a pyrolusite lattice which contains about $P_R \simeq 9\%$ of ramsdellite motifs. Finally, the refinement results in an apparent size of crystallites of about ~90 Å, which is in agreement with SEM observations.

In an attempt to improve this refinement, we explored the effect of anisotropic particle size by varying the number of layers stacked along the *c* axis or the width of the layer in the *ab* plane, but, as previously mentioned, this did not improve the quality of the refinement. In particular, the two small reflections at around $2\theta_{Cu} \simeq 40.0°$ were less well accounted for (see Fig. SI10). We also explored the possibility of having clusters or extended domains of ramsdellite structure included in a pyrolusite matrix by means of explicit stacking (as opposed to random stacking), but without additional improvement. In the same way, we discarded the presence of ε-MnO_2 as a secondary phase, as suggested by previous reports on electrochemically active manganese oxides (Balachandran *et al.*, 2003; Kim *et al.*, 2006). Finally, we examined the effect of twinning on the XRD patterns of the pyrolusite from a series of simulations using *FAULTS*. The modifications

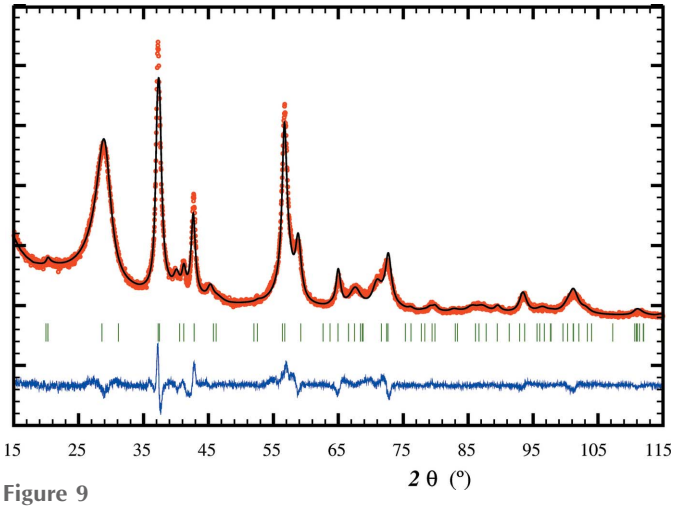

Figure 9
FAULTS refinement of the XRD pattern of the MnO_2 sample. The red circles, the black line and the blue line represent the observed, calculated and difference patterns, respectively. The vertical green bars show the positions of the Bragg reflections of the average cell.

Table 3
Refined structural model of the sample of MnO_2.

Cell: a = 4.378 (1), b = 2.870 (1), c = 4.445 (1) Å, α = 90, β = 90, γ = 90°.

Pyrolusite-type layers.

	Atom	x/a	y/b	z/c	B_{iso} (Å^2)	Occupancy
Layer r1	Mn^{IV+}	0	0	0	0.90 (1)	1.0
	O^{II-}	0.27 (1)	0	0.32 (1)	0.09 (1)	1.0
	O^{II-}	0.73 (1)	0	−0.32 (1)	0.09 (1)	1.0
	O^{II-}	0.82 (1)	$\frac{1}{2}$	0.21 (1)	0.09 (1)	1.0
	O^{II-}	0.18 (1)	$\frac{1}{2}$	−0.21 (1)	0.09 (1)	1.0
Layer r2	Mn^{IV+}	$\frac{1}{2}$	$\frac{1}{2}$	0	0.90 (1)	1.0

Ramsdellite-type layers.

	Atom	x/a	y/b	z/c	B_{iso} (Å^2)	Occupancy
Layer R1	Mn^{IV+}	−0.01 (1)	$\frac{3}{4}$	0.30 (1)	0.90 (1)	1.0
	Mn^{IV+}	0.01 (1)	$\frac{1}{4}$	−0.30 (1)	0.90 (1)	1.0
	O^{II-}	0.24 (1)	$\frac{1}{4}$	0.04 (1)	0.09 (1)	1.0
	O^{II-}	0.76 (1)	$\frac{3}{4}$	−0.04 (1)	0.09 (1)	1.0
	O^{II-}	0.33 (1)	$\frac{3}{4}$	0.59 (1)	0.09 (1)	1.0
	O^{II-}	0.67 (1)	$\frac{1}{4}$	−0.59 (1)	0.09 (1)	1.0
	O^{II-}	0.70 (1)	$\frac{1}{4}$	0.39 (1)	0.09 (1)	1.0
	O^{II-}	0.30 (1)	$\frac{3}{4}$	−0.39 (1)	0.09 (1)	1.0
Layer R2	Mn^{IV+}	0.51 (1)	$\frac{3}{4}$	0.29 (1)	0.90 (1)	1.0
	Mn^{IV+}	0.49 (1)	$\frac{1}{4}$	−0.29 (1)	0.90 (1)	1.0
	O^{II-}	0.21 (1)	$\frac{1}{4}$	0.03 (1)	0.09 (1)	1.0
	O^{II-}	0.79 (1)	$\frac{3}{4}$	−0.03 (1)	0.09 (1)	1.0

Transition vectors.

	Transition	x/a	y/b	z/c	Probability	Type
From layer r1	r1 → r1	–	–	–	0	Forbidden
	r1 → r2	0	0	$\frac{1}{2}$	0.908 (1)	Pyrolusite
	r1 → R1	–	–	–	0	Forbidden
	r1 → R2	0	$\frac{1}{4}$	0.789 (1)	0.092 (1)	de Wolff
From layer r2	r2 → r1	0	0	$\frac{1}{2}$	0.908 (1)	Pyrolusite
	r2 → r2	–	–	–	0	Forbidden
	r2 → R1	0	$-\frac{1}{4}$	0.789 (1)	0.092 (1)	de Wolff
	r2 → R2	–	–	–	0	Forbidden
From layer R1	R1 → r1	–	–	–	0	Forbidden
	R1 → r2	0	$-\frac{1}{4}$	0.789 (1)	0.976 (1)	de Wolff
	R1 → R1	–	–	–	0	Forbidden
	R1 → R2	0	0	1.075 (1)	0.024 (1)	Ramsdellite
From layer R2	R2 → r1	0	$\frac{1}{4}$	0.789 (1)	0.976 (1)	de Wolff
	R2 → r2	–	–	–	0	Forbidden
	R2 → R1	0	0	1.075 (1)	0.024 (1)	Ramsdellite
	R2 → R2	–	–	–	0	Forbidden

induced in the XRD patterns do not match the features of the MnO_2 sample studied herein (see Fig. SI11) since the small reflection at around $2\theta_{Cu} \simeq 40.0°$ does not appear for any of the twinned pyrolusite patterns simulated and the (101) pyrolusite reflection splits at lower 2θ angles even for a small degree of twinning. This is in agreement with Chabre & Pannetier's (1995) conclusion on pyrolusite-like heat-treated manganese oxides. However, as rightly pointed out by several groups (Chabre & Pannetier, 1995; Hahn *et al.*, 2013), besides their structural complexity, manganese oxides are known to be nonstoichiometric and to contain substantial amounts of intercalated species (*e.g.* alkali cations, hydroxyl groups, water molecules *etc.*); our ideal MnO_2 stoichiometry assumed for the refinement presented herein is likely not to be strictly true, although deviations are expected to be minor and therefore to have little impact in the diffraction pattern. Despite this approximation the final results of our *FAULTS* refinement are of good quality and provide for the first time a quantitative estimation of the contents of each structural motif (pyrolusite *versus* ramsdellite).

4. Summary, conclusions and outlook

FAULTS is a program which permits the refinement of the X-ray and neutron powder diffraction patterns of any material presenting planar defects (*e.g.* stacking faults, twinning *etc.*). The program has been upgraded to increase its capabilities and make it more accessible to non-initiated users. The new features of the program include the *DIFFaX2FAULTS* converter (which automatically converts *DIFFaX* input files into *FAULTS* files), the visualization of the structural model, new instrumental parameters, the treatment of background and secondary phases, and a new minimization algorithm.

The refinement possibilities of the program were tested against a simulated pattern of a defective $Li_xNi_{1.02}O_2$ sample, as well as the experimental XRD patterns of Li_2PtO_3 and MnO_2 samples. The first example proved the speed and reliability of the refinement process. The second one illustrates the use of secondary phases in the refinement. The last example led to the first quantitative analysis of ramsdellite motifs in a pyrolusite structure.

It is expected that the program will be enriched in the future with additional features aimed at strengthening the refinement process, such as a true quantitative phase analysis and the averaging of calculated diffraction patterns corresponding to different stacking sequences.

5. Download

The *FAULTS* program can be obtained either as part of the *FullProf Suite* at http://www.ill.eu/sites/fullprof/ or as a separate program by downloading the compressed file at http://www.cicenergigune.com/faults/. The source code is also available in the CrysFML repository at http://forge.epn-campus.eu/projects/crysfml/repository/show/Program_Examples/Faults (Rodríguez-Carvajal & Gonzalez-Platas, 2003*a*,*b*). Individual packages containing *FAULTS* executables for different platforms (Windows, Linux and MacOS) together with documentation and examples can also be obtained from http://forge.epn-campus.eu/projects/crysfml/files.

APPENDIX *A*

For the sake of completeness, we provide here a summary of the general expressions for calculating the kinematical intensity of a set of N layers of which there are M distinct types (for more details see Treacy *et al.*, 1991, and references therein).

Each layer of type i has a scattering density $\rho_i(\mathbf{r})$ about an arbitrary origin. We define the probability α_{ij} that an i-type layer is followed by a j-type layer with origin with respect to the origin of the layer i given by the vector $\mathbf{R}_{ij}$. A crystal constructed as a sequence of layers $i, j, k, l, \ldots$ has a scattering density given by

$$V^{(N)}_{ijkl\ldots}(\mathbf{r}) = \rho_i(\mathbf{r}) + \rho_j(\mathbf{r}-\mathbf{R}_{ij}) + \rho_k(\mathbf{r}-\mathbf{R}_{ij}-\mathbf{R}_{jk}) + \rho_l(\mathbf{r}-\mathbf{R}_{ij}-\mathbf{R}_{jk}-\mathbf{R}_{kl}) + \cdots. \quad (2)$$

The probability of that sequence is given by the product $g_i\alpha_{ij}\alpha_{jk}\alpha_{kl}\ldots$ in which g_i is the probability that the i-type layer exists. The following restrictions hold:

$$g_i = \sum_j g_j\alpha_{ji}, \quad \sum_i g_i = 1, \quad \sum_j \alpha_{ji} = 1. \quad (3)$$

Using the reciprocal space vector variable $\mathbf{s}$ (scattering vector) for the kinematic approximation we can write the scattering amplitude as the Fourier transform of (2):

$$\begin{aligned}\phi^{(N)}_{ijkl\ldots}(\mathbf{s}) &= \int V^{(N)}_{ijkl\ldots}(\mathbf{r})\exp(-2\pi i\mathbf{s}\cdot\mathbf{r})\,\mathrm{d}\mathbf{r}\\ &= F_i(\mathbf{s}) + F_j(\mathbf{s})\exp(-2\pi i\mathbf{s}\cdot\mathbf{R}_{ij})\\ &\quad + F_k(\mathbf{s})\exp[-2\pi i\mathbf{s}\cdot(\mathbf{R}_{ij}+\mathbf{R}_{jk})]\\ &\quad + F_l(\mathbf{s})\exp[-2\pi i\mathbf{s}\cdot(\mathbf{R}_{ij}+\mathbf{R}_{jk}+\mathbf{R}_{kl})] + \cdots, \end{aligned} \quad (4)$$

where $F_i(\mathbf{s})$ is the form factor (structure factor) of the i-type layer. The scattering intensity for a statistical ensemble of all possible permutations (M^N) of layers is given by the weighted sum

$$I(\mathbf{s}) = \sum_{i,j,k,l,\ldots} g_i\alpha_{ij}\alpha_{jk}\alpha_{kl}\ldots\phi^{(N)*}_{ijkl\ldots}(\mathbf{s})\phi^{(N)}_{ijkl\ldots}(\mathbf{s}). \quad (5)$$

Explicitly writing out expression (4) in (5) and after some algebraic manipulations one arrives at the equation

$$I(\mathbf{s}) = \sum_{m=0}^{N-1}\sum_i g_i[F_i^*(\mathbf{s})\,\phi_i^{(N-m)}(\mathbf{s}) + F_i(\mathbf{s})\phi_i^{(N-m)*}(\mathbf{s}) - |F_i(\mathbf{s})|^2]. \quad (6)$$

To obtain this equation we have used the following recursive relation:

$$\phi_i^{(N)}(\mathbf{s}) = F_i(\mathbf{s}) + \sum_j \alpha_{ij}\exp(-2\pi i\mathbf{s}\cdot\mathbf{R}_{ij})\phi_j^{(N-1)}(\mathbf{s}) \quad (7)$$

with $\phi_i^{(0)}(\mathbf{s}) = 0$. The expression for the intensity can be further simplified using matrix notation and realizing that we obtain a geometrical series that can be readily summed. We define the following matrices:

Column matrices:

$$\mathbf{\Phi}^{(N)} = [\phi_i^{(N)}(\mathbf{s})], \quad \mathbf{F} = [F_i(\mathbf{s})], \quad \mathbf{G} = [g_iF_i(\mathbf{s})]. \quad (8)$$

Square matrices:

$$\mathbf{T} = [\alpha_{ij}\exp(-2\pi i\mathbf{s}\cdot\mathbf{R}_{ij})], \quad \mathbf{I} = \text{identity}. \quad (9)$$

Using the superscript T for transpose, the superscript -1 for inverse and the quantity (appearing as a final step in the calculation of a geometric series)

$$\begin{aligned}\mathbf{\Psi}^{(N)} &= \frac{1}{N}(\mathbf{I}-\mathbf{T})^{-1}[(N+1)\mathbf{I} - (\mathbf{I}-\mathbf{T})^{-1}(\mathbf{I}-\mathbf{T}^{N+1})]\mathbf{F}\\ &= (\mathbf{I}-\mathbf{T})^{-1}\mathbf{F}',\\ \mathbf{\Psi}^{(N)} &= \mathbf{F}' + \mathbf{T}\mathbf{\Psi}^{(N)},\\ \mathbf{F}' &= \frac{1}{N}[(N+1)\mathbf{I} - (\mathbf{I}-\mathbf{T})^{-1}(\mathbf{I}-\mathbf{T}^{N+1})]\mathbf{F},\end{aligned} \quad (10)$$

we obtain the normalized intensity per layer in the compact and closed form

$$I_N(\mathbf{s}) = \frac{I(\mathbf{s})}{N} = \mathbf{G}^{*\mathrm{T}}\mathbf{\Psi}^{(N)} + \mathbf{G}^{\mathrm{T}}\mathbf{\Psi}^{(N)*} - \mathbf{G}^{*\mathrm{T}}\mathbf{F}. \quad (11)$$

For a powder sample we have to take the powder average of (11) by performing a surface integration in reciprocal space for constant $s = |\mathbf{s}|$ shells. This is done numerically within the calculation kernel of *DIFFaX* that we use in *FAULTS*. After multiplying by the Lorentz–polarization factor $\mathrm{Lp}(s)$, we obtain the resulting function $I_{\mathrm{Pow}}(s)$ as

$$\begin{aligned}I_{\mathrm{Pow}}(s) &= \mathrm{Lp}(s)\int\!\!\int_{|\mathbf{s}|=s} I_N(\mathbf{s})\,\mathrm{d}\Sigma_s\\ &= \mathrm{Lp}(s)\int\!\!\int_{|\mathbf{s}|=s} I_N(s,\vartheta,\varphi)\,s^2\sin\vartheta\,\mathrm{d}\vartheta\,\mathrm{d}\varphi.\end{aligned} \quad (12)$$

This function is directly transformed to the 2θ space within the numerical integration procedure. Let us call the result $I_{\mathrm{Pow}}(2\theta)$. This quantity is finally convoluted with the instrumental resolution function $g(2\theta)$ that we assume to be a Voigt profile with a full width at half-maximum following a Cagliotti-like (Caglioti *et al.* 1958) dependency on the scattering angle. The profile intensity is finally given by the expression

$$y(2\theta,\boldsymbol{\alpha}) = S\,I_{\mathrm{Pow}}(2\theta,\mathbf{c}) * g(2\theta,\mathbf{p}) + b(2\theta,\mathbf{b}), \quad (13)$$

in which * indicates convolution product, S is a scale factor and $b(2\theta,\mathbf{b})$ is the background function, which takes into account all other components of the diffraction pattern that are not described by the modelled diffraction pattern of the faulted sample $I_{\mathrm{Pow}}(2\theta)$. The arrays $\alpha = \{\mathbf{c},\mathbf{p},\mathbf{b}\}$ contain the list of all free parameters of the global model. The set of parameters $\mathbf{c}$ of the faulted model contains the scale factor, atom positions within the layers, atomic displacement parameters, transition probabilities, stacking vectors with their corresponding anisotropic displacements parameters *etc.* (see the manual of *FAULTS* for details).

The model for the instrumental function is a Thompson–Cox–Hasting (Thompson *et al.* 1987) pseudo-Voigt function approximating the full Voigt function $V(2\theta, H_{\mathrm{G}}, H_{\mathrm{L}})$, which includes components for spherical size effects to handle effects of coherence domains in all directions. The Gaussian, H_{G}, and Lorentzian, H_{L}, full widths at half-maximum measured in degrees are assumed to have the following dependency on θ:

$$\begin{aligned}H^2_{\mathrm{G}}(2\theta,U,V,W,D_{\mathrm{G}}) &= U\tan^2\theta + V\tan\theta + W + \left(\frac{180}{\pi}\right)^2\frac{4\ln 2\lambda^2}{\pi D^2_{\mathrm{G}}\cos^2\theta},\\ H_{\mathrm{L}}(2\theta,X,D_{\mathrm{L}}) &= X\tan\theta + \frac{180}{\pi}\frac{2\lambda}{\pi D_{\mathrm{L}}\cos\theta}.\end{aligned} \quad (14)$$

The profile refinable parameters are constituted by the set $\mathbf{p} = \{U, V, W, X, D_G, D_L\}$. In the case of refinement of a diffraction pattern with two wavelengths, the peak profile is assumed to be formed by normalized Voigt doublets.

The background function $b(2\theta, \mathbf{b})$ can contain secondary phases and a real background modelled by linear interpolation or by a Chebychev polynomial:

$$b(2\theta, \mathbf{b}) = B_{\rm ckg}(2\theta, \mathbf{b}_{\rm ckg}) + \sum_{\phi} S_{\phi} y_{{\rm calc},\phi}(2\theta). \qquad (15)$$

The secondary phases are provided in external files that have been previously produced by using *FullProf* in simulation mode without background. There is a scale factor S_ϕ associated with each secondary ϕ phase provided as a contributing profile and specific background parameters $\mathbf{b}_{\rm ckg}$ in a number that depends on the degree of the polynomial, so that if Np is the number of additional phases, $\mathbf{b} = \{\mathbf{b}_{\rm ckg}, \{S_\phi\}_{\phi=1,\ldots,{\rm Np}}\}$ is the subset of parameters concerning background and secondary phases.

Presently the program calculates the relative area of the full diffraction pattern of each component; however, a true quantitative phase analysis is not yet possible.

Acknowledgements

The authors are grateful to SAFT for kindly providing the γ-MnO_2 sample. Financial support was provided by the Ministerio de Economia y Competitividad (MINECO) of the Spanish Government through grant ENE2013-44330-R. MR acknowledges the Spanish Ministerio de Economía y Competitividad (MINECO) for her postdoctoral fellowship (Juan de la Cierva-Formación, 2014, reference number FJCI-2014-19990). The structures were drawn and examined with the help of the visualization programs *FullProf Studio* (Rodríguez-Carvajal & Chapon, 2004) and *VESTA* (Momma & Izumi, 2011). The XRD patterns were plotted using the GUI program *WinPLOTR* (Rodríguez-Carvajal & Roisnel, 1998; Roisnel & Rodríquez-Carvajal, 2001) included in the *FullProf Suite* (Rodríguez-Carvajal, 1993*a*,*b*).

References

Balachandran, D., Morgan, D., Ceder, G. & van de Walle, A. (2003). *J. Solid State Chem.* **173**, 462–475.
Bolzan, A., Fong, C., Kennedy, B. & Howard, C. (1993). *Aust. J. Chem.* **46**, 939–944.
Boulineau, A., Croguennec, L., Delmas, C. & Weill, F. (2009). *Chem. Mater.* **21**, 4216–4222.
Bréger, J., Jiang, M., Dupré, N., Meng, Y. S., Shao-Horn, Y., Ceder, G. & Grey, C. P. (2005). *J. Solid State Chem.* **178**, 2575–2585.
Caglioti, G., Paoletti, A. & Ricci, F. P. (1958). *Nucl. Instrum.* **3**, 223–228.
Casas-Cabanas, M., Rodríguez-Carvajal, J., Canales-Vázquez, J., Laligant, Y., Lacorre, P. & Palacín, M. R. (2007). *J. Power Sources*, **174**, 414–420.
Casas-Cabanas, M., Rodríguez-Carvajal, J., Canales-Vázquez, J. & Palacín, M. R. (2006). *J. Mater. Chem.* **16**, 2925–2939.
Casas-Cabanas, M., Rodríguez-Carvajal, J. & Palacín, M. R. (2006). *Z. Kristallogr. Suppl.* **23**, 243–248.
Chabre, Y. & Pannetier, J. (1995). *Prog. Solid State Chem.* **23**, 1–130.
Charenton, J. C. & Strobel, P. (1988). *J. Solid State Chem.* **77**, 33–39.
Croguennec, L., Pouillerie, C. & Delmas, C. (2000*a*). *Solid State Ionics*, **135**, 259–266.
Croguennec, L., Pouillerie, C. & Delmas, C. (2000*b*). *J. Electrochem. Soc.* **147**, 1314–1321.
Croguennec, L., Pouillerie, C., Mansour, A. N. & Delmas, C. (2001). *J. Mater. Chem.* **11**, 131–141.
Delmas, C., Fouassier, C. & Hagenmuller, P. (1980). *Phys. B+C*, **99**, 81–85.
Delmas, C., Pérès, J. P., Rougier, A., Demourgues, A., Weill, F., Chadwick, A., Broussely, M., Perton, F., Biensan, P. & Willmann, P. (1997). *J. Power Sources*, **68**, 120–125.
Hahn, B. P., Long, J. W. & Rolison, D. R. (2013). *Acc. Chem. Res.* **46**, 1181–1191.
Jouanneau, S., Sarciaux, S., Le Gal La Salle, A. & Guyomard, D. (2001). *Solid State Ionics*, **140**, 223–232.
Kiefer, F., Karttunen, A. J., Döblinger, M. & Fässler, T. F. (2011). *Chem. Mater.* **23**, 4578–4586.
Kim, C.-H., Akase, Z., Zhang, L., Heuer, A. H., Newman, A. E. & Hughes, P. J. (2006). *J. Solid State Chem.* **179**, 753–774.
Knížek, K., Jirák, Z., Hejtmánek, J., Brázda, P., Buršík, J., Soroka, M. & Beran, P. (2015). *J. Solid State Chem.* **229**, 160–163.
Leoni, M., Gualtieri, A. F. & Roveri, N. (2004). *J. Appl. Cryst.* **37**, 166–173.
Matsunaga, T., Komatsu, H., Shimoda, K., Minato, T., Yonemura, M., Kamiyama, T., Kobayashi, S., Kato, T., Hirayama, T., Ikuhara, Y., Arai, H., Ukyo, Y., Uchimoto, Y. & Ogumi, Z. (2016*a*). *Chem. Mater.* **28**, 4143–4150.
Matsunaga, T., Komatsu, H., Shimoda, K., Minato, T., Yonemura, M., Kamiyama, T., Kobayashi, S., Kato, T., Hirayama, T., Ikuhara, Y., Arai, H., Ukyo, Y., Uchimoto, Y. & Ogumi, Z. (2016*b*). *J. Phys. Chem. Lett.* **7**, 2063–2067.
McCalla, E., Abakumov, A., Rousse, G., Reynaud, M., Sougrati, M. T., Budic, B., Mahmoud, A., Dominko, R., Van Tendeloo, G., Hermann, R. & Tarascon, J. (2015). *Chem. Mater.* **27**, 1699–1708.
McCalla, E., Abakumov, A. M., Saubanère, M., Foix, D., Berg, E. J., Rousse, G., Doublet, M.-L., Gonbeau, D., Novák, P., Van Tendeloo, G., Dominko, R. & Tarascon, J. M. (2015). *Science*, **350**, 1516–1521.
Momma, K. & Izumi, F. (2011). *J. Appl. Cryst.* **44**, 1272–1276.
Ohzuku, T., Ueda, A. & Nagayama, M. (1993). *J. Electrochem. Soc.* **140**, 1862–1870.
O'Malley, M. J. (2009). PhD thesis, The Ohio State University, Columbus, OH, USA.
O'Malley, M. J., Verweij, H. & Woodward, P. M. (2008). *J. Solid State Chem.* **181**, 1803–1809.
Post, J. E. & Heaney, P. J. (2004). *Am. Mineral.* **89**, 969–975.
Rodríguez-Carvajal, J. (1993*a*). *FullProf Suite*, http://www.ill.eu/sites/fullprof/.
Rodríguez-Carvajal, J. (1993*b*). *Phys. B Condens. Matter*, **192**, 55–69.
Rodríguez-Carvajal, J. & Chapon, L. (2004). *FullProf Studio*, http://www.ill.eu/sites/fullprof/.
Rodríguez-Carvajal, J. & Gonzalez-Platas, J. (2003*a*). *CrysFML*, http://forge.epn-campus.eu/projects/crysfml/repository/.
Rodríguez-Carvajal, J. & Gonzalez-Platas, J. (2003*b*). *IUCr Commission on Crystallographic Computing Newsletter*, No. 1, pp. 50–58.
Rodríguez-Carvajal, J. & Roisnel, T. (1998). *WinPLOTR*, http://www.ill.eu/sites/fullprof/ and http://www.cdifx.univ-rennes1.fr/winplotr/.
Roisnel, T. & Rodríguez-Carvajal, J. (2001). *Mater. Sci. Forum*, **378–381**, 118–123.
Rougier, A., Gravereau, P. & Delmas, C. (1996). *J. Electrochem. Soc.* **143**, 1168–1175.
Shunmugasundaram, R., Arumugam, R. S. & Dahn, J. R. (2016). *J. Electrochem. Soc.* **163**, A1394–A1400.
Thompson, P., Cox, D. E. & Hastings, J. B. (1987). *J. Appl. Cryst.* **20**, 79–83.
Treacy, M. M. J., Newsam, J. M. & Deem, M. W. (1991). *Proc. R. Soc. London Ser. A*, **433**, 499–520.
Wolff, P. M. de (1959). *Acta Cryst.* **12**, 341–345.